Layer 2/3 Pyramidal Neurons Control the Gain of Cortical Output

Michael Quiquempoix, Sophie L Fayad, Katia Boutourlinsky, Nathalie Leresche, Régis C. Lambert, Thomas Bessaïh

Report

Cell Reports

Layer 2/3 Pyramidal Neurons Control the Gain of Cortical Output

Graphical Abstract

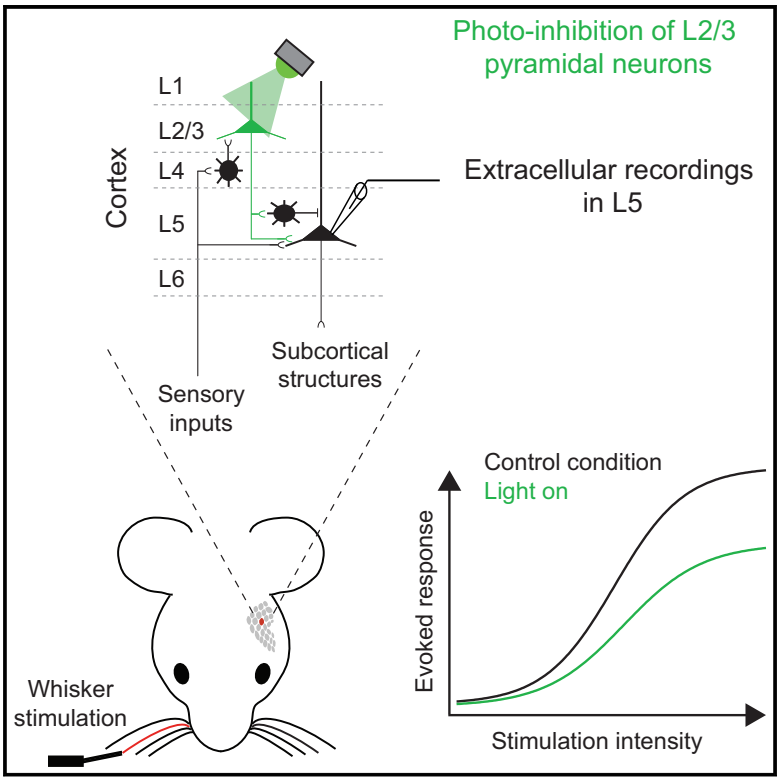

Authors

Michael Quiquempoix, Sophie L. Fayad, Katia Boutourlinsky, Nathalie Leresche, Régis C. Lambert, Thomas Bessaih

Correspondence

thomas.bessaih@upmc.fr

In Brief

Quiquempoix et al. investigated the role of the canonical cortical layer 2/3 (L2/3)-to-L5 pathway in sensory processing by deep-layer neurons of the mouse somatosensory cortex. They show that the recruitment of this pathway plays a major role in amplifying sensory-evoked responses in L5 neurons.

Highlights

- Cortical layer 2/3 (L2/3) input evokes both excitatory and inhibitory currents in L5
- L2/3 input has a net excitatory effect in L5
- L2/3 input amplifies sensory-evoked responses in L5
- L2/3 input modulates the gain of sensory-evoked responses in L5

Quiquempoix et al., 2018, Cell Reports *24*, 2799–2807
September 11, 2018
https://doi.org/10.1016/j.celrep.2018.08.038

CellPress

Cell Reports
Report

Layer 2/3 Pyramidal Neurons Control the Gain of Cortical Output

Michael Quiquempoix,[1] Sophie L. Fayad,[1] Katia Boutourlinsky,[1] Nathalie Leresche,[1,2] Régis C. Lambert,[1,2] and Thomas Bessaih[1,2,3,*]
[1]Sorbonne Université, CNRS, INSERM, Neurosciences Paris Seine – Institut de Biologie Paris Seine (NPS-IBPS), 75005 Paris, France
[2]Senior author
[3]Lead Contact
*Correspondence: thomas.bessaih@upmc.fr
https://doi.org/10.1016/j.celrep.2018.08.038

SUMMARY

Initial anatomical and physiological studies suggested that sensory information relayed from the periphery by the thalamus is serially processed in primary sensory cortical areas. It is thought to propagate from layer 4 (L4) up to L2/3 and down to L5, which constitutes the main output of the cortex. However, more recent experiments point toward the existence of a direct processing of thalamic input by L5 neurons. Therefore, the role of L2/3 neurons in the sensory processing operated by L5 neurons is now highly debated. Using cell type-specific and reversible optogenetic manipulations in the somatosensory cortex of both anesthetized and awake mice, we demonstrate that L2/3 pyramidal neurons play a major role in amplifying sensory-evoked responses in L5 neurons. The amplification effect scales with the velocity of the sensory stimulus, indicating that L2/3 pyramidal neurons implement gain control in deep-layer neurons.

INTRODUCTION

Although a striking feature of primary sensory cortical areas is their vertical division into six layers, the role of such laminar organization in sensory processing is not fully understood (Douglas and Martin, 2007; Harris and Shepherd, 2015). Pioneering anatomical reconstruction of physiologically identified neurons suggested the existence of a canonical circuit model within which sensory information is serially processed (Gilbert and Wiesel, 1979). In this model, sensory information is first preprocessed in layer 4 (L4), which constitutes the main thalamo-recipient layer. Then preprocessed signals are sent up to L2/3, which constitute the main output of L4 excitatory neurons. After another processing step in L2/3 recurrent networks, signals propagate down to L5 neurons, which drive subcortical structures involved in action such as the basal ganglia, the colliculus, and the spinal cord (Douglas and Martin, 2004).

However, many anatomical and physiological experiments revealed that thalamocortical axons also innervate deep-layer neurons, which challenges the serial model (Bureau et al., 2006; Freund et al., 1985; Humphrey et al., 1985; Wimmer et al., 2010). More important, several *in vivo* studies demonstrated that sensory-evoked responses could be elicited in L5 neurons in the absence of L2/3 activation (Constantinople and Bruno, 2013; Huang et al., 1998; Schwark et al., 1986). Therefore, the role of L2/3 neurons in the sensory processing operated by L5 neurons remains to be established.

L2/3 pyramidal neurons are a direct source of excitatory input to L5 pyramidal neurons (Lefort et al., 2009; Petreanu et al., 2007), but they also indirectly inhibit them by activating GABAergic neurons located in either L2/3 or L5 (Adesnik and Scanziani, 2010). As a consequence, the scale and the sign of the modulation of L5 firing by L2/3 pyramidal neurons ultimately depend on the interactions and balance between di-synaptic feedforward inhibition and monosynaptic excitation, which might be activity dependent (Pouille and Scanziani, 2004).

In the present study, we used cell type-specific and reversible optogenetic manipulations to investigate the activity-dependent properties of L2/3-to-L5 pathway *in vitro* and its contribution to the sensory processing operated by L5 neurons in the somatosensory cortex of both anesthetized and awake mice.

RESULTS

ChR2-Mediated Photostimulation of L2/3 Pyramidal Neurons

To achieve temporally precise and reversible activation of L2/3 pyramidal neurons, we introduced the light-sensitive cation channel channelrhodopsin-2 (ChR2-Venus) (Nagel et al., 2003) together with GFP in a region that includes the left primary somatosensory cortex (S1) using *in utero* electroporation (IUE) (Figure 1A, left) (Saito and Nakatsuji, 2001). We histologically confirmed that the expression of the opsin was restricted to L2/3 pyramidal neurons and their axons, with no expression in the somata of neurons located in other layers (Figure 1A, middle). In L4, the density and path of the axons were such that gaps in fluorescence shaping barrels were visible (Figure 1A, middle). As expected, 99.2% of fluorescent neurons had pyramidal morphology (Figure 1A, right; n = 3,185 cells from four animals), and overall, 19.48 ± 0.03% of L2/3 neurons (identified by anti-NeuN immuno-staining) also expressed fluorescence in the GFP emission band (Figure 1B).

To confirm that ChR2 formed functional membrane channels, we performed whole-cell recordings from GFP-positive neurons

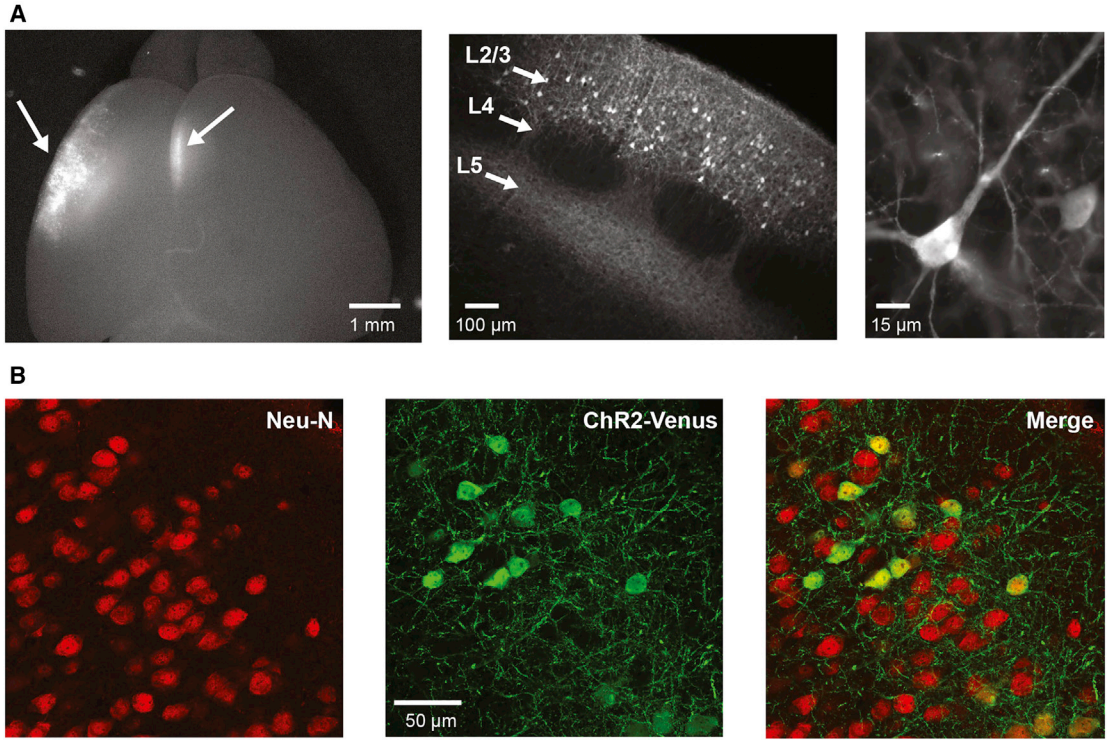

Figure 1. ChR2 Expression in L2/3 Pyramidal Neurons following *In Utero* Electroporation

(A) Left: GFP fluorescence in a whole brain of an electroporated mouse with ChR2-Venus and GFP plasmids (scale bar, 1 mm). Arrows indicate S1 (left) and callosal projections (right). Middle: GFP/Venus fluorescence in a coronal slice through the barrel cortex of an electroporated hemisphere showing somato-dendritic labeling in L2/3 and axonal branches in L2/3 and L5 (scale bar, 100 μm). Right: labeled L2/3 pyramidal neuron (scale bar, 15 μm).

(B) Double immunostaining for ChR2-Venus and the neuronal marker NeuN (scale bar, 50 μm).

See also Figure S1.

in slices from P21–P43 mice that had undergone IUE (n = 8 neurons from seven animals; Figure S1). Neurons were held at −70 mV in the voltage-clamp configuration in the presence of the glutamate receptor blocker CNQX (10 μM) to avoid contaminations from synaptically evoked activities. Brief (5 ms) pulses of blue (470 nm) light (5–10 mW) at different frequencies (3–70 Hz) were applied at the surface of the slice. Such stimulations elicited inward currents (> 200 pA) in all GFP-positive neurons (Figure S1C). To evaluate the efficiency of these currents at evoking action potentials, we recorded the neurons in the current-clamp configuration (Figure S1D). For each stimulation frequency, we calculated the probability of evoking action potentials as a function of the pulse number in the train (Figure S1E). Photostimulations reliably evoked action potentials in electroporated neurons only up to 30 Hz. Therefore, we did not use higher stimulation frequencies in subsequent experiments.

Activity-Dependent Modulation of L5 Neuron Firing by L2/3 Pyramidal Neurons

A previous study demonstrated that photo-initiated gamma band (around 30 Hz) oscillatory activity drives both excitatory pos-synaptic currents (EPSCs) and inhibitory post-synaptic currents (IPSCs) in L5 pyramidal neurons (Adesnik and Scanziani, 2010). However, it is possible that excitatory and inhibitory synapses exhibit different short-term plasticity. Therefore, the balance between excitatory and inhibitory conductances evoked in L5 pyramidal neurons might depend on the frequency of L2/3 activity patterns. To address this point, we performed whole-cell recordings from morphologically identified regular spiking L5 pyramidal neurons while initiating synchronous activities at different frequencies in L2/3 pyramidal neurons with light stimulations (n = 19 neurons from 13 animals; Figures 2A–2C).

We first recorded the neurons in the voltage-clamp configuration at the IPSC reversal potential (around −70 mV) and at the EPSC reversal potential (0 to +10 mV) to isolate EPSCs and IPSCs, respectively (Figure 2D). Regardless of the stimulation frequency of L2/3 pyramidal neurons, L5 pyramidal neurons received both excitation and inhibition (Figure 2F). Furthermore, the excitatory and inhibitory charges increased as a function of stimulation frequency (Pearson correlation coefficients [R] of 0.97 and −0.95 for IPSC and EPSC charges, respectively).

Both excitation and inhibition were sensitive to bath applied CNQX (10 μM) in all tested neurons (n = 4), which indicates their synaptic origin (Figures S2A and S2B). IPSCs followed EPSCs by 1.8 ± 0.9 ms, which is consistent with a di-synaptic nature of the inhibition (Figure 2D, right). Indeed, photostimulation of L2/3 pyramidal neurons strongly activated non-pyramidal fast-spiking neurons in L5 (Figures S2C–S2F; n = 9 neurons from six animals), which are the most prevalent cell type among neocortical inhibitory interneurons (Steriade, 2004). However, while the

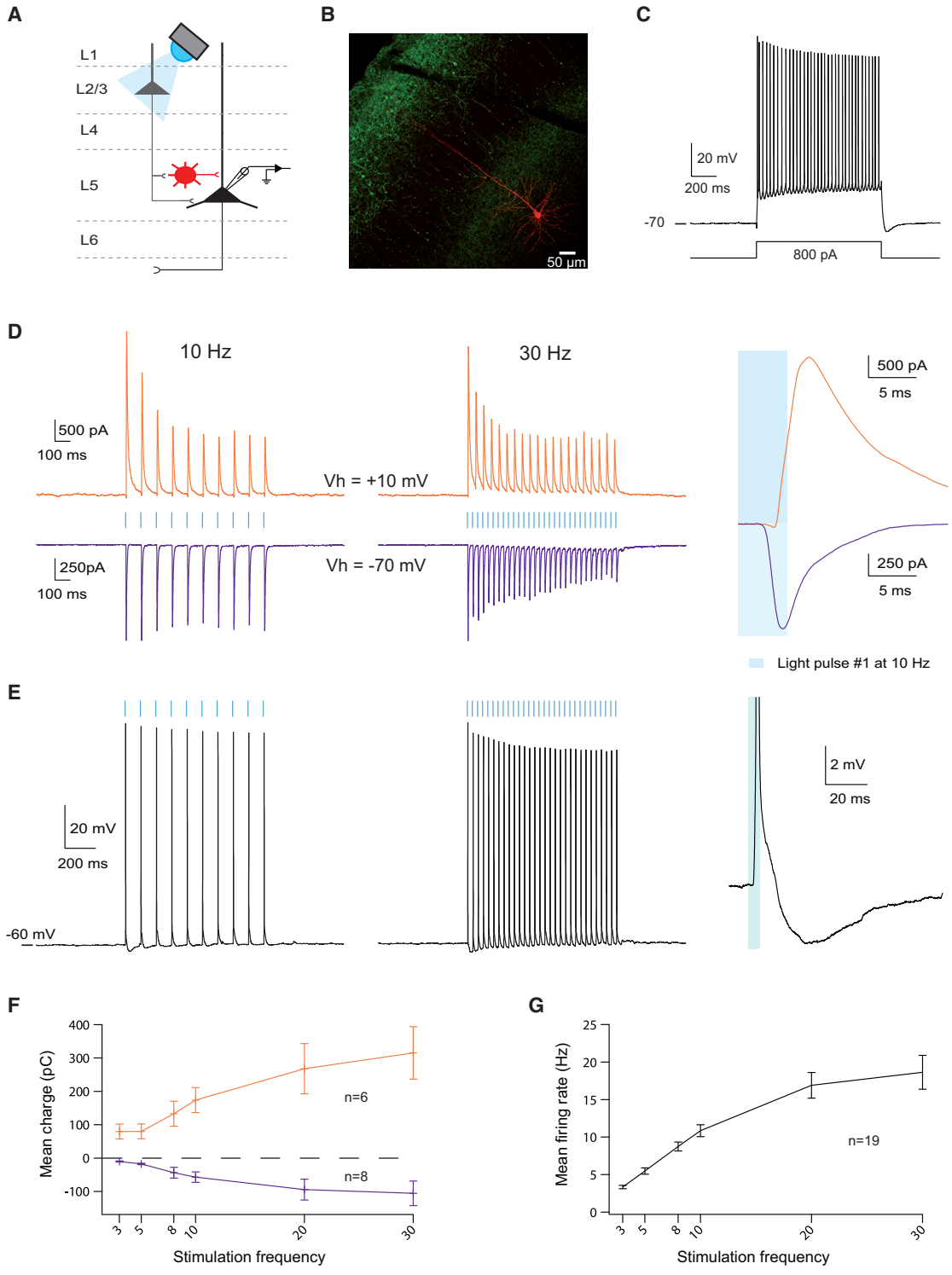

Figure 2. Modulation of L5 Pyramidal Neuron Firing by L2/3 Input

(A) Schema of the experimental paradigm. Whole-cell recordings were performed in L5 pyramidal neurons while photo-stimulating L2/3 pyramidal neurons.

(B) High-resolution image showing the biocytin labeling (red) of an individual L5 pyramidal neuron (scale bar, 50 µm).

(C) Regular spiking adapting firing pattern in response to a current pulse for the neuron shown in (B).

(D). Examples of EPSCs (purple traces; recorded at −70 mV) and IPSCs (orange traces; recorded at +10 mV) evoked in the neuron shown in (B) by the photostimulation of L2/3 pyramidal neurons. Right: enlargement of the first evoked currents at 10 Hz.

(legend continued on next page)

recruitment of these neurons might underlie the evoked IPSCs in L5 pyramidal neurons, the involvement of other classes of inhibitory neurons cannot be ruled out.

To address how the combination of the two types of evoked conductances affects the neuronal spiking of L5 pyramidal neurons, we performed recordings in the current-clamp configuration. Membrane potentials were held close to −65mV, a level comparable with what has been observed *in vivo* (Constantinople and Bruno, 2011). Regardless of the stimulation frequency, light pulses invariably induced an increase in the spiking activity that weakly adapted for the duration of the stimulus (Figures 2E and 2G). This result demonstrates that L2/3 pyramidal neurons can exert a powerful excitatory influence on L5 pyramidal neurons at all tested stimulation frequencies (3–30 Hz).

Arch-Mediated Photo-Suppression of Sensory-Evoked Responses in L2/3 Pyramidal Neurons

Next, we investigated whether L2/3 input is involved in the sensory processing operated by L5 neurons. Therefore, we designed an approach to specifically and reversibly inactivate L2/3 pyramidal neurons while recording sensory-evoked responses in deep-layer neurons.

To achieve fast and reversible inactivation of L2/3 pyramidal neurons, we transfected them with the light-sensitive proton pump archaerhodopsin (ArchT-GFP) (Han et al., 2011). In close similarity to what we observed for the ChR2, the expression of ArchT was restricted to L2/3 pyramidal neurons and their axons (Figure S3A), and overall, 20.3 ± 0.07% of L2/3 neurons (identified by anti-NeuN immuno-staining) also expressed fluorescence in the GFP emission band (Figure S3B).

To confirm that ArchT formed functional membrane pumps, we performed whole-cell recordings from GFP-positive neurons in slices from P20–P22 mice that had undergone IUE (Figures S3C and S3D). Neurons were held at membrane potentials at which they exhibit sustained discharges (6–12 Hz), and green (530 nm) light pulses (2–5 mW) were flashed at the surface of the slices via an optical fiber. In all neurons (n = 8 from three animals), light pulses (1 s duration at 0.1 Hz) evoked large (33.23 ± 3.78 mV), reliable, and reversible hyperpolarizations associated with a complete suppression of the spiking activity (Figures S3E and S3F).

To assess the efficiency of light pulses at suppressing L2/3 sensory-evoked responses, electroporated mice were anesthetized, and a craniotomy was performed above the ArchT-expressing barrel cortex. Then, tetrodes were lowered to depths between 200 and 350 μm, which corresponds to L2/3 (Figure S4B), and using filtering procedures and cluster-cutting algorithms, we isolated single-unit spiking activities (Figures S4C–SF4).

Somatosensory stimulations were elicited by mechanically deflecting the principal whisker (PW) in the rostrocaudal direction with 1 s cosine waves at 30 Hz (Figure S4A, bottom trace). In the control condition, these stimulations elicited sustained increases in firing rates that were not different in terms of magnitude and temporal profile from those observed in unelectroporated animals (Figures S4F, S4H, and S4I; p = 0.27, Wilcoxon rank-sum test).

To activate ArchT, we used 2 s green light pulses (starting 0.5 s before the onset of sensory stimuli), as we wanted to avoid paradoxical vesicle release associated with prolonged illumination of ArchT-expressing axon terminals (Mahn et al., 2016). As illustrated for the example recording in Figure S4F, the magnitude of the evoked responses was lower when sensory stimuli were paired with light pulses.

On a unit-by-unit basis, 63% of L2/3 units exhibited a significant reduction in sensory-evoked mean firing rate (MFR) during the photo-suppression condition ($p < 0.05$, Wilcoxon rank-sum test; n = 22 of 35 units from four animals; Figure S4G). The remaining units showed no significant change ($p > 0.05$, Wilcoxon rank-sum test), potentially reflecting the fact that only a fraction of L2/3 pyramidal neurons was transfected. For suppressed units, the average reduction was 35.7 ± 3.6%, demonstrating the effectiveness of our optogenetic approach.

L2/3 Pyramidal Neuron Activity Amplifies Sensory-Evoked Responses in L5 Neurons

Next, we investigated the functional impact of decreasing L2/3 neuronal spiking activity on the sensory processing operated by deep-layer neurons. As shown in Figure 3, light-induced decrease of L2/3 activity caused a significant reduction in the firing rate of 72% of the recorded L5 neurons during sensory stimulation ($p < 0.05$, Wilcoxon rank-sum test; n = 36 of 50 units from ten animals; Figure 3F). The remaining units showed no significant change ($p > 0.05$, Wilcoxon rank-sum test). For suppressed units, the magnitude of the suppression was 30.2 ± 2.2%. The suppression effect was not due to direct light-emitting diode (LED) illumination of the retina or the cortex, as it was absent in unelectroporated animals ($p < 0.05$, Wilcoxon rank-sum test; n = 27 units from four animals; Figure 3G).

Anesthesia may change the impact of L2/3 pyramidal neurons on sensory-evoked responses in L5 neurons. To address this issue, we optogenetically suppressed sensory-evoked activity in L2/3 pyramidal neurons of awake head-fixed mice habituated to run on a free-spinning circular treadmill (Video S1). In this condition, 55% of L5 units exhibited a significant light-induced decrease in firing rate during sensory stimulation ($p < 0.05$, Wilcoxon rank-sum test; n = 21 of 40 units from four animals; Figure 3H). Again, the remaining units showed no significant change ($p > 0.05$, Wilcoxon rank-sum test). On average, the magnitude of the suppression was 27.4 ± 2.8%, which is slightly lower than what we observed in anesthetized animals. However, this

(E) Examples of evoked spiking activity for the neuron shown in (B) in response to the photostimulation of L2/3 pyramidal neurons. Right: enlargement of the membrane potential fluctuations evoked at the onset of a stimulation at 10 Hz. For clarity, the action potential was clipped.
(F) Plots of average excitatory (purple curve) and inhibitory (orange curve) charges evoked in L5 pyramidal neurons as a function of the photostimulation frequency of L2/3 pyramidal neurons. Error bars indicate ±SEM.
(G) Plots of the average mean firing rate evoked in L5 pyramidal neurons as a function of the photostimulation frequency of L2/3 pyramidal neurons. Error bars indicate ±SEM.
See also Figure S2.

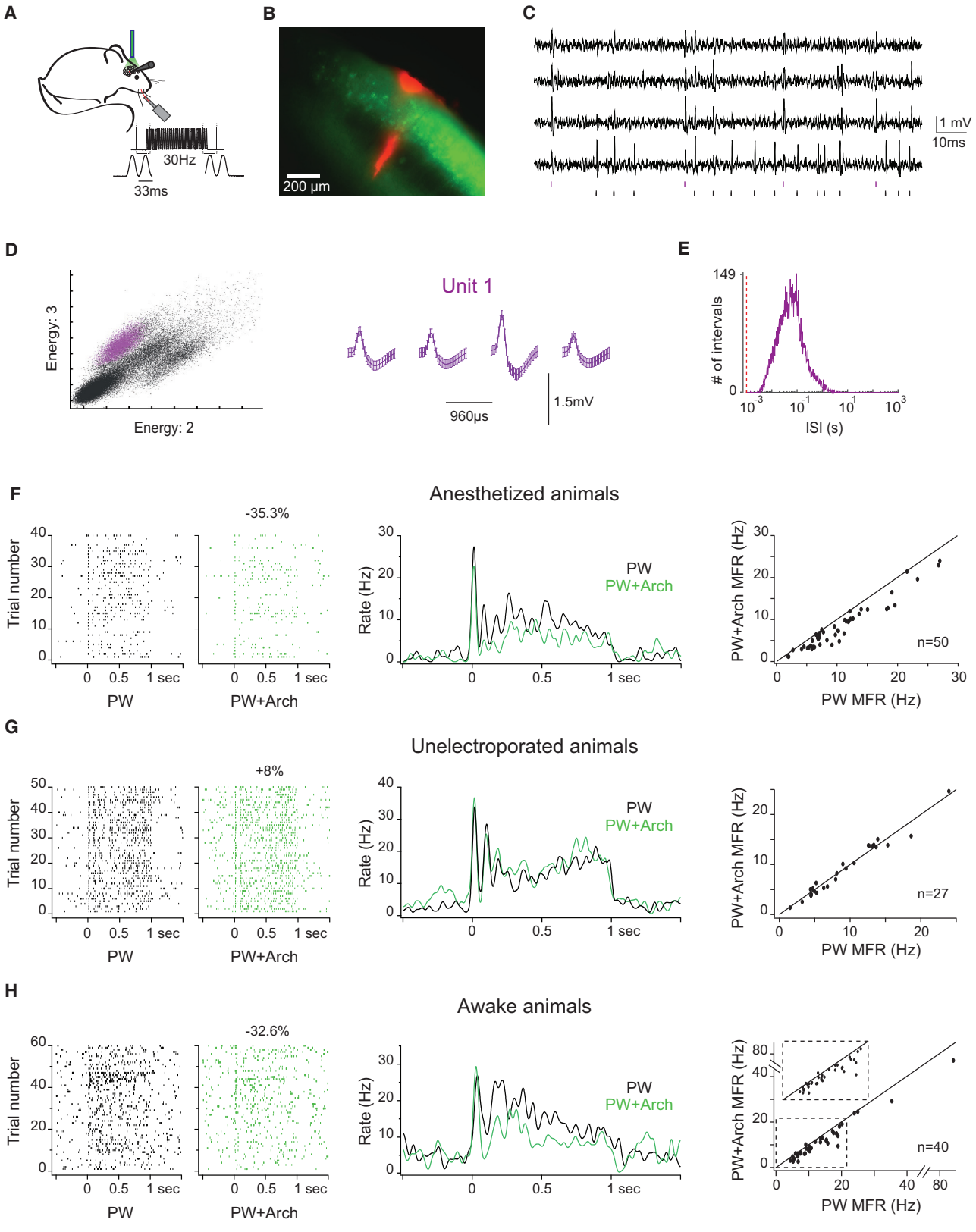

(legend on next page)

difference was not statistically significant ($p > 0.37$, Wilcoxon rank-sum test). Therefore, L2/3 pyramidal neurons amplify sensory-evoked responses in L5 in both anesthetized and awake conditions.

Gain Control of Sensory-Evoked Responses in L5 by L2/3 Pyramidal Neurons

The recruitment of L2/3 pyramidal neurons should also modify the relationship between the firing of L5 neurons and stimulus intensity (input-output function). To address this point, we first characterized the response of L5 units to cosine waves stimulations of increasing velocity in the control condition ($n = 11$). As shown for the representative example in Figure 4A, the relationships between the evoked spiking activity and the velocity of the stimulation showed saturation and were well fitted by a sigmoidal function (Figure 4B, black curve).

When decreasing L2/3 input with light pulses, we observed stimulus-dependent suppression in response magnitude; that is, it became larger at increasing stimulus velocity (Figure 4B, green curve). The transformation between the spiking activity in control and photo-suppression conditions was better achieved by a multiplicative scaling model (blue dashed curve) than an additive model (yellow dashed curve), indicating a gain change (Haider and McCormick, 2009). The fact that scaled multiplication qualitatively better fits L2/3 modulation of input-output relations than addition was observed for every L5 unit and also at the level of the normalized population response (Figure 4C).

Furthermore, across all units, we found that light pulses significantly decreased the maximal response magnitude (Rmax) of the sigmoidal fit ($p = 0.00098$, paired Wilcoxon signed rank test; Figure 4D) without affecting half-saturation stimulus velocity (C_{50}) ($p = 0.083$, paired Wilcoxon signed rank test; Figure 4E). This result is also consistent with a gain change, such that the amplification of sensory-evoked responses in L5 by L2/3 input scales multiplicatively with the stimulus velocity.

DISCUSSION

Our finding might seem inconsistent with a recent study indicating that pharmacological inactivation of L2/3 activity has no impact on the magnitude of sensory-evoked responses in L5 neurons of rat barrel cortex (Constantinople and Bruno, 2013). However, it is important to note that Constantinople and Bruno (2013) studied cortical responses to transient ramp and hold stimulations, whereas we used sustained tactile stimuli. Therefore, one may hypothesize that the amplification effect of sensory-evoked responses in L5 by L2/3 activity described here is not relevant for isolated transient sensory stimulations. Indeed, recent work in the mouse visual cortex highlighted the fact that, at least in anesthetized animals, cortical recurrent networks contribute to sensory-evoked activities only after the first 43 ms of the responses (Reinhold et al., 2015). Therefore, it is likely that, in freely behaving animals, the recruitment of the translaminar connectivity is task dependent.

How might L2/3 pyramidal neurons control the gain of L5 neurons? Although various combinations of cellular mechanisms can lead to changes in the gain of a target neuron, our *in vitro* intracellular recordings indicate that the major mechanism by which L2/3 neurons influence L5 neurons firing is through the generation of excitatory post-synaptic potentials, irrespective of their activity patterns (Figure 2). In the absence of spontaneous membrane potential fluctuations, as is the case *in vitro*, the membrane depolarization produced by such excitatory post-synaptic potentials should affect the integration of thalamic inputs in L5 neurons by shifting the threshold of the input-output relationship leftward along the input axis and, therefore, does not result in a purely multiplicative scaling of the gain curve. However, *in vivo*, cortical neurons are constantly bombarded by synaptic inputs, which induces spontaneous large membrane potential fluctuations (Destexhe et al., 2003). As a consequence, the average firing rate as a function of the membrane potential depolarization evoked by sensory stimulations follows a power-law function (Priebe and Ferster, 2012). Modeling and experimental studies indicate that in such a condition, a simple depolarization of cortical neurons by a few millivolts and its associated drop in input resistance, as occurs in L5 neurons following the stimulation of L2/3 input, can induce a multiplicative gain modulation of the responses to sensory stimuli (Cardin et al., 2008; Murphy and Miller, 2003).

Gain modulation is a widespread neuronal operation that is found in many brain regions (Silver, 2010). In particular, sensory-evoked responses in cortex can be gain modulated by contextual information, such as body position, expectation, or the state of vigilance (Salinas and Thier, 2000). Although this modulation is thought to play a major role in the performance

Figure 3. Photo-Suppression of L2/3 Pyramidal Neurons Decreases the Magnitude of Sensory-Evoked Responses in L5 Neurons

(A) Schema of the experimental paradigm. Recordings were made in the barrel cortex while stimulating the principal whisker of the recorded units using a piezoelectric device. Top trace: stimulus waveform, as measured with photodiodes. Bottom traces: cutouts of the onset and offset of the stimulus waveform.

(B) Example image of a DiI track left by a recording electrode inserted into the barrel cortex. Green, Arch-GFP; red, DiI. Scale bar, 200 μm.

(C) Band-pass-filtered (0.6–6 kHz) signals from the four wires of a tetrode. Raster plots for one isolated unit (purple) and unclustered spikes (black) are shown at the bottom.

(D) Example of a tetrode recording in which one unit was isolated. The scatterplot represents the energy of spikes on two channels of a tetrode. Assigned spikes to one unit are in purple (unassigned spikes are in black). The average waveforms from each of the recording sites for the sorted unit are shown on the right.

(E) Inter-spike-interval (ISI) histograms of the clustered unit showing refractory periods. Red line indicates 1 ms.

(F–H) Peri-stimulus time raster plots and histograms of representative L5 units to 30 Hz whisker stimulations presented either alone (left) or paired with green light pulses (middle): anesthetized (F), unelectroporated (G), and awake (H) animals. Stimulations of the principal whisker (PW) start at 0 and last 1 s. For the raster plots, each line corresponds to one trial, and each dot corresponds to the occurrence of an action potential. Note the decrease in the spike count when whisker stimulations are paired with green light pulses in electroporated animals. Right: plots of the evoked mean firing rates (MFRs) when the sensory stimuli were paired with light pulses (PW+Arch) versus the control condition (PW) for all the recorded units.

See also Figures S3 and S4.

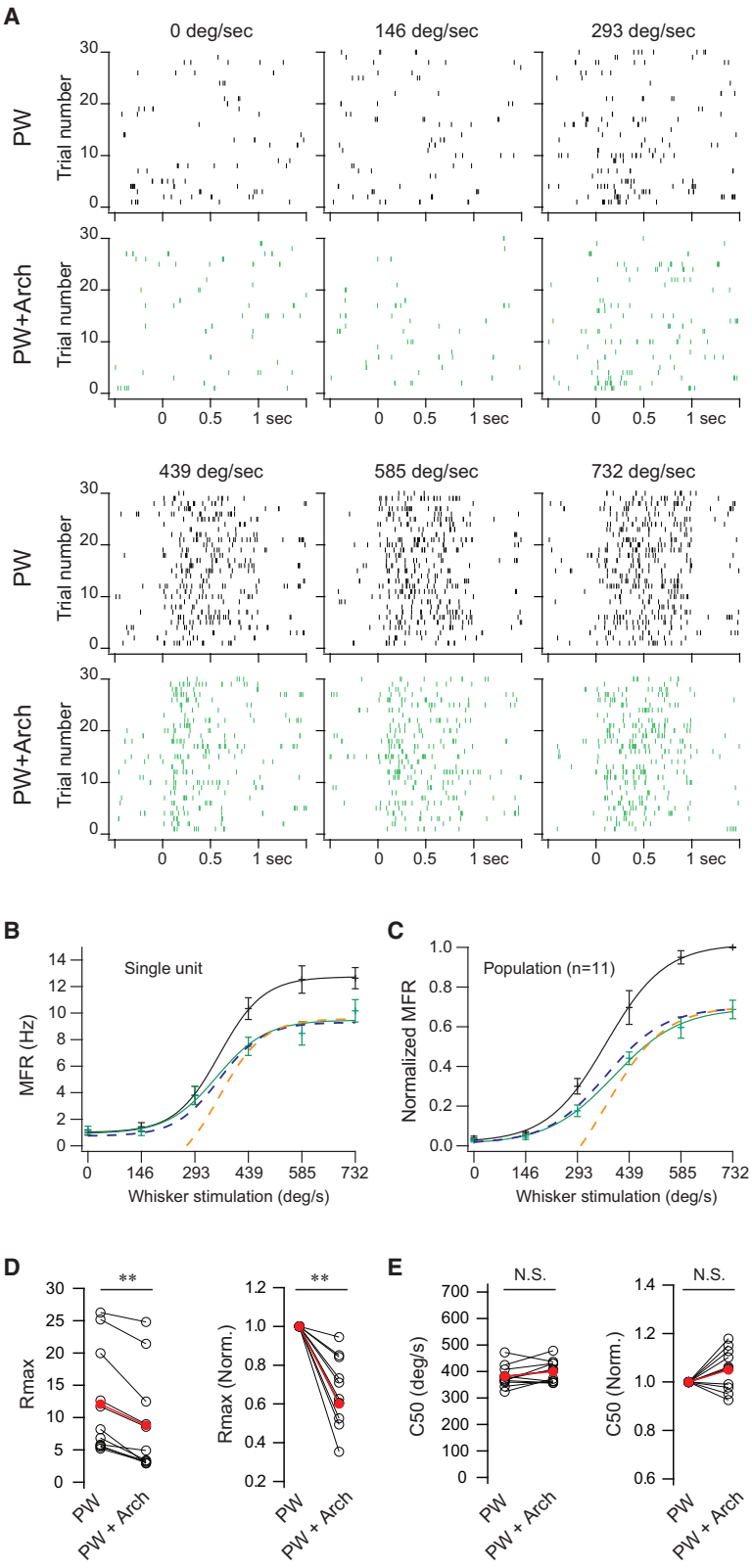

Figure 4. Gain Modulation of Sensory-Evoked Responses in L5 by L2/3 Input

(A) Peri-stimulus time raster plots illustrate the spiking response of a representative L5 unit to repeated 30 Hz whisker stimulations of increasing velocity. Rasters in black correspond to the control condition (PW). Rasters in green correspond to the condition in which sensory stimuli were paired with green light pulses (PW+Arch).

(B) Evoked mean firing rate (MFR) as a function of stimulus velocity for the unit shown in (A). Black curve corresponds to the sigmoidal fit in the control condition, and green curve corresponds to the sigmoidal fit when sensory stimuli were paired with light pulses. Error bars indicate ±SEM. Blue dashed curve was obtained by dividing the control curve by a constant to match the maximal response magnitude (Rmax) of the photo-suppression condition curve. Yellow dashed curve was obtained by subtracting the control curve by a constant to match the Rmax of the photo-suppression condition.

(C) Same as in (B) for the whole recorded neuronal population. Data from all units have been normalized to the maximum firing rate obtained under the control conditions, averaged, and fitted. Error bars indicate ±SEM.

(D) Effects of L2/3 suppression on the Rmax. Black lines indicate the evolution of Rmax for individual units (n = 11). Red lines correspond to the mean values. Raw Rmax values are shown on the left, and normalized values are shown on the right. $^{**}p < 0.001$.

(E) Effects of L2/3 suppression on the half-saturation stimulus velocity (C_{50}). Black lines indicate the evolution of C_{50} for individual units (n = 11). Red lines correspond to the mean values. Raw C_{50} values are shown on the left, and normalized values are shown on the right. NS, not significant.

of subjects to discriminate between different stimuli (McAdams and Maunsell, 1999), little is known about the circuits underlying its implementation. Our results indicate that the canonical L2/3-to-L5 pathway may contribute to the implementation of this major computational operation in cortical networks. Importantly, L2/3 activity in barrel cortex is not only driven by input from L4 but also modulated by long-range connections from other cortical areas, such as the secondary somatosensory cortex (S2) or primary motor cortex (M1) (Ni and Chen, 2017). Although M1 inputs provide S1 neurons with motor context during object localization tasks (Petreanu et al., 2012), inputs from S2 carry choice-related information during tactile detection tasks (Yang et al., 2016). Furthermore, L2/3 neurons are extremely sensitive to neuromodulatory cholinergic and adrenergic inputs (Polack et al., 2013), whose activities vary with the level of arousal (Harris and Thiele, 2011). Therefore, L2/3 pyramidal neurons constitute a key target for controlling the gain of cortical output according to contextual information.

STAR★METHODS

Detailed methods are provided in the online version of this paper and include the following:

- KEY RESOURCES TABLE
- CONTACT FOR REAGENT AND RESOURCE SHARING
- EXPERIMENTAL MODEL AND SUBJECT DETAILS
- METHOD DETAILS
  - *In utero* electroporation
  - Slice preparation
  - *In vitro* electrophysiological recordings
  - Surgery and preparation for *in vivo* electrophysiological recordings in anesthetized animals
  - Surgery and preparation for *in vivo* electrophysiological recordings in awake animals
  - *In vivo* electrophysiological recordings
  - Histology
- QUANTIFICATION AND STATISTICAL ANALYSIS

SUPPLEMENTAL INFORMATION

Supplemental Information includes four figures and one video and can be found with this article online at https://doi.org/10.1016/j.celrep.2018.08.038.

ACKNOWLEDGMENTS

This work was supported by ANR GoFT and FRC et les Rotariens de France, Espoir en Tête 2012. M.Q. was supported by Région Ile de France DIM Cerveau et Pensée. pCAGGS-ChR2-Venus, pAAV-CAG-ArchT-GFP, and pCAG-GFP plasmids were gifts from Karel Svoboda, Edward Boyden, and Connie Cepko, respectively.

AUTHOR CONTRIBUTIONS

Conceptualization, T.B.; Investigation, M.Q., S.L.F., and K.B.; Writing – Original Draft, T.B.; Writing – Review & Editing, T.B., N.L., R.C.L., M.Q., and S.L.F.; Supervision, T.B.; Funding Acquisition, N.L and R.C.L.

DECLARATION OF INTERESTS

The authors declare no competing interests.

Received: November 27, 2017
Revised: May 28, 2018
Accepted: August 13, 2018
Published: September 11, 2018

REFERENCES

Adesnik, H., and Scanziani, M. (2010). Lateral competition for cortical space by layer-specific horizontal circuits. Nature *464*, 1155–1160.

Bureau, I., von Saint Paul, F., and Svoboda, K. (2006). Interdigitated paralemniscal and lemniscal pathways in the mouse barrel cortex. PLoS Biol. *4*, e382.

Cardin, J.A., Palmer, L.A., and Contreras, D. (2008). Cellular mechanisms underlying stimulus-dependent gain modulation in primary visual cortex neurons in vivo. Neuron *59*, 150–160.

Constantinople, C.M., and Bruno, R.M. (2011). Effects and mechanisms of wakefulness on local cortical networks. Neuron *69*, 1061–1068.

Constantinople, C.M., and Bruno, R.M. (2013). Deep cortical layers are activated directly by thalamus. Science *340*, 1591–1594.

Destexhe, A., Rudolph, M., and Paré, D. (2003). The high-conductance state of neocortical neurons in vivo. Nat. Rev. Neurosci. *4*, 739–751.

Douglas, R.J., and Martin, K.A.C. (2004). Neuronal circuits of the neocortex. Annu. Rev. Neurosci. *27*, 419–451.

Douglas, R.J., and Martin, K.A.C. (2007). Mapping the matrix: the ways of neocortex. Neuron *56*, 226–238.

Freund, T.F., Martin, K.A., and Whitteridge, D. (1985). Innervation of cat visual areas 17 and 18 by physiologically identified X- and Y- type thalamic afferents. I. Arborization patterns and quantitative distribution of postsynaptic elements. J. Comp. Neurol. *242*, 263–274.

Gilbert, C.D., and Wiesel, T.N. (1979). Morphology and intracortical projections of functionally characterised neurones in the cat visual cortex. Nature *280*, 120–125.

Haider, B., and McCormick, D.A. (2009). Rapid neocortical dynamics: cellular and network mechanisms. Neuron *62*, 171–189.

Han, X., Chow, B.Y., Zhou, H., Klapoetke, N.C., Chuong, A., Rajimehr, R., Yang, A., Baratta, M.V., Winkle, J., Desimone, R., and Boyden, E.S. (2011). A high-light sensitivity optical neural silencer: development and application to optogenetic control of non-human primate cortex. Front. Syst. Neurosci. *5*, 18.

Harris, K.D., and Shepherd, G.M.G. (2015). The neocortical circuit: themes and variations. Nat. Neurosci. *18*, 170–181.

Harris, K.D., and Thiele, A. (2011). Cortical state and attention. Nat. Rev. Neurosci. *12*, 509–523.

Huang, W., Armstrong-James, M., Rema, V., Diamond, M.E., and Ebner, F.F. (1998). Contribution of supragranular layers to sensory processing and plasticity in adult rat barrel cortex. J. Neurophysiol. *80*, 3261–3271.

Humphrey, A.L., Sur, M., Uhlrich, D.J., and Sherman, S.M. (1985). Termination patterns of individual X- and Y-cell axons in the visual cortex of the cat: projections to area 18, to the 17/18 border region, and to both areas 17 and 18. J. Comp. Neurol. *233*, 190–212.

Lefort, S., Tomm, C., Floyd Sarria, J.-C., and Petersen, C.C.H. (2009). The excitatory neuronal network of the C2 barrel column in mouse primary somatosensory cortex. Neuron *61*, 301–316.

Mahn, M., Prigge, M., Ron, S., Levy, R., and Yizhar, O. (2016). Biophysical constraints of optogenetic inhibition at presynaptic terminals. Nat. Neurosci. *19*, 554–556.

Matsuda, T., and Cepko, C.L. (2004). Electroporation and RNA interference in the rodent retina in vivo and in vitro. Proc. Natl. Acad. Sci. U S A *101*, 16–22.

McAdams, C.J., and Maunsell, J.H.R. (1999). Effects of attention on the reliability of individual neurons in monkey visual cortex. Neuron *23*, 765–773.

Murphy, B.K., and Miller, K.D. (2003). Multiplicative gain changes are induced by excitation or inhibition alone. J. Neurosci. *23*, 10040–10051.

Nagel, G., Szellas, T., Huhn, W., Kateriya, S., Adeishvili, N., Berthold, P., Ollig, D., Hegemann, P., and Bamberg, E. (2003). Channelrhodopsin-2, a directly

light-gated cation-selective membrane channel. Proc. Natl. Acad. Sci. U S A *100*, 13940–13945.

Ni, J., and Chen, J.L. (2017). Long-range cortical dynamics: a perspective from the mouse sensorimotor whisker system. Eur. J. Neurosci. *46*, 2315–2324.

Petreanu, L., Huber, D., Sobczyk, A., and Svoboda, K. (2007). Channelrhodopsin-2-assisted circuit mapping of long-range callosal projections. Nat. Neurosci. *10*, 663–668.

Petreanu, L., Gutnisky, D.A., Huber, D., Xu, N.L., O'Connor, D.H., Tian, L., Looger, L., and Svoboda, K. (2012). Activity in motor-sensory projections reveals distributed coding in somatosensation. Nature *489*, 299–303.

Polack, P.-O., Friedman, J., and Golshani, P. (2013). Cellular mechanisms of brain state-dependent gain modulation in visual cortex. Nat. Neurosci. *16*, 1331–1339.

Pouille, F., and Scanziani, M. (2004). Routing of spike series by dynamic circuits in the hippocampus. Nature *429*, 717–723.

Priebe, N.J., and Ferster, D. (2012). Mechanisms of neuronal computation in mammalian visual cortex. Neuron *75*, 194–208.

Reinhold, K., Lien, A.D., and Scanziani, M. (2015). Distinct recurrent versus afferent dynamics in cortical visual processing. Nat. Neurosci. *18*, 1789–1797.

Saito, T., and Nakatsuji, N. (2001). Efficient gene transfer into the embryonic mouse brain using in vivo electroporation. Dev. Biol. *240*, 237–246.

Salinas, E., and Thier, P. (2000). Gain modulation: a major computational principle of the central nervous system. Neuron *27*, 15–21.

Schwark, H.D., Malpeli, J.G., Weyand, T.G., and Lee, C. (1986). Cat area 17. II. Response properties of infragranular layer neurons in the absence of supragranular layer activity. J. Neurophysiol. *56*, 1074–1087.

Silver, R.A. (2010). Neuronal arithmetic. Nat. Rev. Neurosci. *11*, 474–489.

Steriade, M. (2004). Neocortical cell classes are flexible entities. Nat. Rev. Neurosci. *5*, 121–134.

Wimmer, V.C., Bruno, R.M., de Kock, C.P.J., Kuner, T., and Sakmann, B. (2010). Dimensions of a projection column and architecture of VPM and POm axons in rat vibrissal cortex. Cereb. Cortex *20*, 2265–2276.

Yang, H., Kwon, S.E., Severson, K.S., and O'Connor, D.H. (2016). Origins of choice-related activity in mouse somatosensory cortex. Nat. Neurosci. *19*, 127–134.

STAR★METHODS

KEY RESOURCES TABLE

REAGENT or RESOURCE	SOURCE	IDENTIFIER
Antibodies		
Chicken anti-GFP	Aves Labs, Inc	Cat# GFP-1020; RRID: AB_10000240
Mouse anti-NeuN antibody	Millipore	Cat# MAB377; RRID: AB_2298772
Alexa 488 conjugated goat anti-chicken	Invitrogen	Cat# A-11039; RRID: AB_2534096
Alexa-594 conjugated goat anti-mouse	Invitrogen	Cat# A-11032; RRID: AB_2534091
Chemicals, Peptides, and Recombinant Proteins		
Fast Green	Sigma-Aldrich	Cat# F7258; CAS: 2353-45-9
Tris-HCl (pH 8.0)	Sigma-Aldrich	Cat# 07066
Isoflurane	Iso-Vet	Cat# 3248850; GTIN: 18904026625157
Buprenorphine (Buprecare)	Axience	GTIN: 03760087151893
NaCl	Sigma-Aldrich	Cat# S6191; CAS: 7647-14-5
KCl	Sigma-Aldrich	Cat# 60128; CAS: 7447-40-7
$CaCl_2$	Sigma-Aldrich	Cat# C3881; CAS: 10035-04-8
$MgCl_2$	Sigma-Aldrich	Cat# M2670; CAS: 7791-18-6
NaH_2PO_4	Sigma-Aldrich	Cat# S5011; CAS: 7558-80-7
$NaHCO_3$	Sigma-Aldrich	Cat# 31437; CAS: 144-55-8
Glucose	Sigma-Aldrich	Cat# 49159; CAS: 14431-43-7
Potassium gluconate	Sigma-Aldrich	Cat# G4500; CAS: 299-27-4
EGTA	Sigma-Aldrich	Cat# E3889; CAS: 67-42-5
HEPES	Sigma-Aldrich	Cat# H3375; CAS: 7365-45-9
D-APV	Alomone	Cat# D-140; CAS: 79055-68-8
D-mannitol	Sigma-Aldrich	Cat# M9647; CAS: 69-65-8
Disodium ATP	Sigma-Aldrich	Cat# A7699; CAS: 34369-07-8
Disodium GTP	Roche	Cat# 10106399001; CAS: 36051-31-7
Biocytin	Sigma-Aldrich	Cat# B4261; CAS: 576-19-2
Bupivacaine	Henry Schein	Cat# 054879
Fentanyl (Sufenta)	Janssen	GTIN: 7680524130440
Xylazine (Rompun)	Bayer	GTIN: 04007221032311
Baytril	Bayer	GTIN: 04007221031291
Paraformaldehyde in 0.1 M phosphate buffer saline	Electron Microscopy Sciences	Cat# 15710; CAS: 30525-89-4
Sodium azide	Sigma-Aldrich	Cat# S2002; CAS: 26628-22-8
Phosphate buffer saline	Sigma-Aldrich	Cat# D1408
Triton X-100	Sigma-Aldrich	Cat# T8787; CAS: 9002-93-1
Bovine Serum Albumin	Sigma-Aldrich	Cat# A2153; CAS: 9048-46-8
Streptavidin-Rhodamine-RedX	Jackson ImmunoResearch Europe	Cat# 016-290-084
DiI, 10% in ethanol	Invitrogen	Cat# V22885
CNQX	Sigma-Aldrich	Cat# C127; CAS: 115066-14-3
Critical Commercial Assays		
QIAGEN plasmid preparation kits	QIAGEN	Cat# 12362
Kwik-Cast	World Precision Instruments	Cat# KWIK-CAST
Fluoromount medium	Sigma-Aldrich	Cat# F4680
Experimental Models: Organisms/Strains		
C57BL/6JRj mice	Janvier labs	Cat# SC-C57 J-M; RRID: MGI:2670020

(*Continued on next page*)

Continued

REAGENT or RESOURCE	SOURCE	IDENTIFIER
Recombinant DNA		
pCAGGS-ChR2-Venus	Petreanu et al., 2007	Addgene plasmid # 15753
pAAV-CAG-ArchT-GFP	Han et al., 2011	Addgene plasmid # 29777
pCAGGS-ArchT-Venus	This paper	N/A
pCAG-GFP	Matsuda and Cepko, 2004	Addgene plasmid # 11150
Software and Algorithms		
PClamp (version 9)	Molecular Devices	https://www.moleculardevices.com/products/axon-patch-clamp-system/acquisition-and-analysis-software/pclamp-software-suite
Cheetah (version 5)	Neuralynx	https://neuralynx.com/software/cheetah
Igor Pro (version 6)	wavemetrics	https://www.wavemetrics.com
SpikeSort3D (version 2)	Neuralynx	https://neuralynx.com/software/spikesort-3d
ImageJ (version 1)	NIH	https://imagej.nih.gov/ij/download.html
Other		
Quartz-insulated platinum/tungsten (90%/10%) tetrodes	Thomas Recording Gmbh	Cat# AN000259
Piezoelectric bimorph stimulator	Physik Instrumente Gmbh	Cat# PL122.11

CONTACT FOR REAGENT AND RESOURCE SHARING

Further information and requests for resources and reagents should be directed to and will be fulfilled by the Lead Contact, Thomas Bessaih (Thomas.bessaih@upmc.fr).

EXPERIMENTAL MODEL AND SUBJECT DETAILS

All data were collected from C57BL/6JRj mice of either sex from post-natal days 20 to 43. Animals were group housed (from 2 to 5 per cage) with *ad libitum* access to food and water in a 12hr light / dark cycle in a pathogen-free facility maintained at 22–24°C. All experiments were conducted in accordance with the ethical guidelines of the Federation for Laboratory Animal Science Associations (FELASA) and with the approval of the French National Consultative Ethics Committee for health and life sciences (authorization number: 02564.02)

METHOD DETAILS

In utero electroporation

DNA constructs coding for ChR2-Venus, GFP or ArchT3.0-GFP were inserted into pCAGGS vector modified for *in utero* electroporation. DNAs were purified and concentrated using QIAGEN plasmid preparation kits and dissolved in 10 mM Tris-HCl (pH 8.0).

L2/3 progenitor cells were transfected via *in utero* electroporation. Embryonic day 15.5 timed-pregnant mice were anesthetized using an isoflurane-oxygen mixture (2 to 3% of isoflurane in O_2). The uterine horns were exposed, and 1 μL of DNA solution with 0.05 % of Fast Green (Sigma) was pressure injected (Picospritzer, General Valve) through a pulled glass pipette (30–40 μm tip diameter) into the left lateral ventricle of each embryo. The DNA solution contained either a mixture of plasmids encoding ChR2-Venus and GFP in a 3:1 molar ratio or only the plasmid encoding ArchT3.0-GFP. In both cases, final DNA concentration was set to be 2 μg/μl. The head of each embryo was placed between tweezer electrodes (NEPA GENE), with the positive plate contacting the left side of the head. Electroporation was achieved with five square pulses (duration 50 ms, frequency 1 Hz, 45 V). The uterus was then returned to the abdominal cavity, and the abdominal wall and skin were sutured. Buprenorphine was given post-operatively (0.05 mg/kg, twice at 8 hr interval). Pups were born by natural delivery.

GFP fluorescence was used to screen for positive animals under a fluorescent dissecting scope 1 day after birth. Only pups showing strong fluorescence in the GFP emission band in the somatosensory cortex at postnatal day 1 were used in subsequent experiments.

Slice preparation

Mice (3 to 6 weeks) were anesthetized with isoflurane before decapitation. The brain was carefully removed and placed for a few minutes into a 4-8°C bicarbonate-buffered saline (BBS) solution containing (in mM) 125 NaCl, 2.5 KCl, 2 $CaCl_2$, 1 $MgCl_2$, 1.25 NaH_2PO_4, 26 $NaHCO_3$ and 25 glucose (osmolarity: 305 mOsm; pH 7.3 after equilibration with 95% O_2 and 5% CO_2). Coronal

slices (300 μm) were then cut using a vibratome (Leica). The slicing procedure was performed in an ice-cold solution containing (in mM): 130 potassium gluconate, 15 KCl, 2 EGTA, 20 HEPES, 25 glucose, 1 $CaCl_2$ and 6 $MgCl_2$, supplemented with 0.05 D-APV (304 mOsm, pH 7.4 after equilibration). Slices were then transferred for few minutes to a solution containing (in mM): 225 D-mannitol, 2.5 KCl, 1.25 NaH_2PO_4, 25 $NaHCO_3$, 25 glucose, 1 $CaCl_2$ and 6 $MgCl_2$ (310 mOsm, 4-8°C, oxygenated with 95% O_2 / 5%CO_2), and finally stored for the rest of the experimental day at 32°C in oxygenated BBS. For all recordings, slices were continuously perfused with oxygenated BBS at 32°C.

In vitro electrophysiological recordings

Brain slices were screened for electroporated neurons using a filter set that allowed us to detect GFP fluorescence. Neurons were visualized and patched with borosilicate pipettes (resistance 3–5 MOhm). The intracellular solution contained (in mM) 140 potassium gluconate, 3 MgCl2, 10 HEPES, 0.2 EGTA, 4 disodium ATP, 0.3 disodium GTP and 2mg/ml of biocytin (pH 7.3; 300 mOsm). For photo-stimulation/photo-inhibition protocols, we used either a blue (470 nm) or a green LED (530 nm; Prizmatix) to deliver light through a 200 μm optical fiber (0.4 NA) at the surface of the slice.

Patch-clamp electrodes were connected to a Cairn Optopatch amplifier. Protocols and acquisitions were controlled by PClamp software (Molecular Devices). The membrane currents and potentials were filtered by a 4-pole Bessel filter set at a corner frequency of 2 kHz, digitized on-line at a sampling rate of 20 kHz.

Surgery and preparation for *in vivo* electrophysiological recordings in anesthetized animals

Mice (4 to 6 weeks) were anesthetized with isoflurane vaporized in a mixture of oxygen and air (5% for induction, 2% during surgery). Body temperature was maintained at 37°C via a servo-controlled heating blanket and a rectal thermometer (Harvard Apparatus, Holliston, MA). Bupivacaine (subcutaneous) was administered in the regions to be incised 15 min prior to the first incision. Mice were placed in a stereotaxic apparatus and a craniotomy was made directly above the barrel cortex (−1.0 to −2.0 mm A/P, 3.0 to 4.0 mm M/L). To minimize damage during electrode penetration, the dura was resected and the exposed surface was coated with a layer of silicon oil.

After electrodes placement, isoflurane was replaced by fentanyl (10-40 μg/kg, IP) mixed with xylazine (4 mg/kg, IP) in order to maintain the animal in a sedated state. Additional doses of fentanyl (5 μg/kg) were administered every approximately 2 hours. If the animals presented any sign of discomfort, isoflurane (0.25 to 1 %) was added to supplement this anesthesia regime.

Electrodes were inserted into the brain perpendicular to the surface and lowered to layers 2/3 or 5 under visual guidance and based on readings from the micromanipulator (depths: 200 to 300 μm or 550 to 700 μm for layer 2/3 and layer 5 recordings, respectively).

Surgery and preparation for *in vivo* electrophysiological recordings in awake animals

Survival surgeries were performed 1 week before multiple recording sessions. During these surgeries, a headpost was permanently implanted, and a craniotomy over the barrel cortex was performed. The exposed cortex was covered with silicon oil, and the opening resealed using Kwik-Cast (World Precision Instruments). Mice were then injected with 0.05 mg/kg of buprenorphine subcutaneously and monitored daily. They were also given a course of antibiotics through the water supply (BAYTRIL, Bayer) to prevent infection. Animals were allowed to recover for 2 days following implant surgery before they were trained to run on a circular treadmill (Fast-Trac, Bio-Serv). Mice were headposted in place for increasing intervals on each successive day. Mice were trained until they exhibited robust bouts of running activity during each session (5 days on average).

On the day of recording, the seal over the barrel cortex was removed, and tetrodes were lowered as described above. Mice were allowed to run freely and transitioned between passive and active behavioral states. At the end of a recording session, the craniotomy was flushed with saline and sealed again. On subsequent recording days, the craniotomy was flushed with saline before placing the electrode array in a new recording site.

In vivo electrophysiological recordings

Cortical recordings of units were obtained using quartz-insulated platinum/tungsten (90%/10%) tetrodes (~1–2 MOhm, Thomas Recording). 1 to 2 tetrodes were guided independently at 1 μm resolution through a five-channel concentric microdrive head (Head05-cube-305-305-b, Thomas Recording Gmbh) with 305 μm inter-electrode spacing.

Raw signals were filtered (600–6000 Hz; Neuralynx recording systems), amplified (5000x), digitized at 33,657 Hz, and stored with stimulus markers (Cheetah 5 software; Neuralynx). Waveforms crossing set thresholds (250-500 μV) were captured via the A/D card and analyzed offline. Potential single-units were first identified using automated clustering software utilizing peak and trough feature sets (KlustaKwik). These clusters were then examined manually for waveform shape (SpikeSort3D, Neuralynx). Upon examination of the interspike intervals, multi-units clusters were discarded.

For photo-inhibition protocols, we delivered green (530 nm) light pulses through a 1 mm diameter optical fiber (0.4 NA) coupled to a LED (Prizmatix). The tip of the optical fiber was positioned 2 to 4 mm above the exposed surface.

Before recording, whiskers were trimmed to approximately 6-7 mm. Individual whiskers were mechanically deflected using a ceramic piezoelectric bimorph stimulator (Physik Instrumente Gmbh). For each recording, a glass capillary glued to the end of the stimulator was positioned so that a single whisker rested snugly inside it. The tip of the capillary was positioned approximately 4 to 5 mm from the skin. The whisker was mechanically deflected in the rostrocaudal direction (250 μm) by applying cosine waves

(30 Hz) of 1 s duration to the stimulator. Stimuli were delivered at a rate of 0.2 Hz. The identity of the principal whisker was determined for each animal based on the cortical multi-unit activities. The whisker that evoked the response with the shortest onset latency and the largest number of action potentials was considered to be the principal whisker (PW). Depending on the recording session, we applied 30 to 60 trials per stimulus condition. Single units were included in the analysis if their responses were > 1 Hz and had short onset latency (< 25 ms).

Histology

Mice (3 to 6 weeks) were deeply anesthetized, decapitated and the brain was removed. Brains were post-fixed for 2 to 3 days with 4% paraformaldehyde in 0.1 M phosphate buffer saline (PBS). Then, 60 μM coronal sections were cut with a vibratome (Microm) and kept in PBS solution containing 0.02% of sodium azide.

Sections were washed three times in phosphate buffer saline 0.1 M (PBS) and incubated with 0.2% Triton X-100 and 3% Bovine Serum Albumin (BSA) for 1 hour at room temperature. Then, chicken anti-GFP primary antibody was incubated overnight at room temperature (1:500; Aves Labs, Inc). To determine the fraction of electroporated cells, sections were also stained with mouse anti-NeuN antibody (1:500, Millipore).

Sections were then washed another three times in PBS and incubated for 2 hours at room temperature with Alexa 488 conjugated goat anti-chicken secondary antibody (1:500, Invitrogen) either alone or with Alexa-594 conjugated goat anti-mouse secondary antibody (1: 500, Invitrogen).

For the revelation of biocytin-filled neurons, slices were fixed in 4% paraformaldehyde in PBS (0.1 M), overnight at 4°C, directly after *in vitro* recordings. They were kept in PBS with 0.02% azide to preserve them until immunostaining. Streptavidin-Rhodamine-RedX (1:1000) was added during incubation with goat anti-chicken secondary antibody.

Sections were rinsed 3 times in PBS and mounted in Fluoromount medium. Images were obtained using confocal microscopy (Leica TCS SP5).

In some of the *in vivo* electrophysiological recordings, before insertion, the rear of the tetrodes was painted with fluorescent 1,1'-dioctadecyl- 3,3,3′,3′-tetramethyl indocarbocyanine perchlorate (DiI, 10% in ethanol, Invitrogen). As this dye is a lipophilic neuronal tracer, it allowed assessment of the recording depth. Immediately after euthanasia, the brain was removed, and 300 to 400 μm-thick coronal sections of the barrel cortex were cut with a vibratom in cold PBS. Sections were then mounted in Fluoromount medium.

QUANTIFICATION AND STATISTICAL ANALYSIS

Igor Pro software v6 (wavemetrics) was used for the quantification of all the recordings and the statistical analysis. To avoid making assumptions about the distribution of the data, non-parametric statistics were used. Therefore, between conditions comparison was based on a Wilcoxon rank-sum test (Mann-Whitney U test) for unpaired data or Wilcoxon signed-rank test for paired data. Differences were considered significant if the P value was lower than 0.05. Exact P values of the statistical tests, the number of units and animals can be found in the results sections. All error bars correspond to SEM. All the collected data were included for the quantification and the statistical analysis.

Cell Reports, Volume *24*

Supplemental Information

Layer 2/3 Pyramidal Neurons Control the Gain of Cortical Output

Michael Quiquempoix, Sophie L. Fayad, Katia Boutourlinsky, Nathalie Leresche, Régis C. Lambert, and Thomas Bessaih

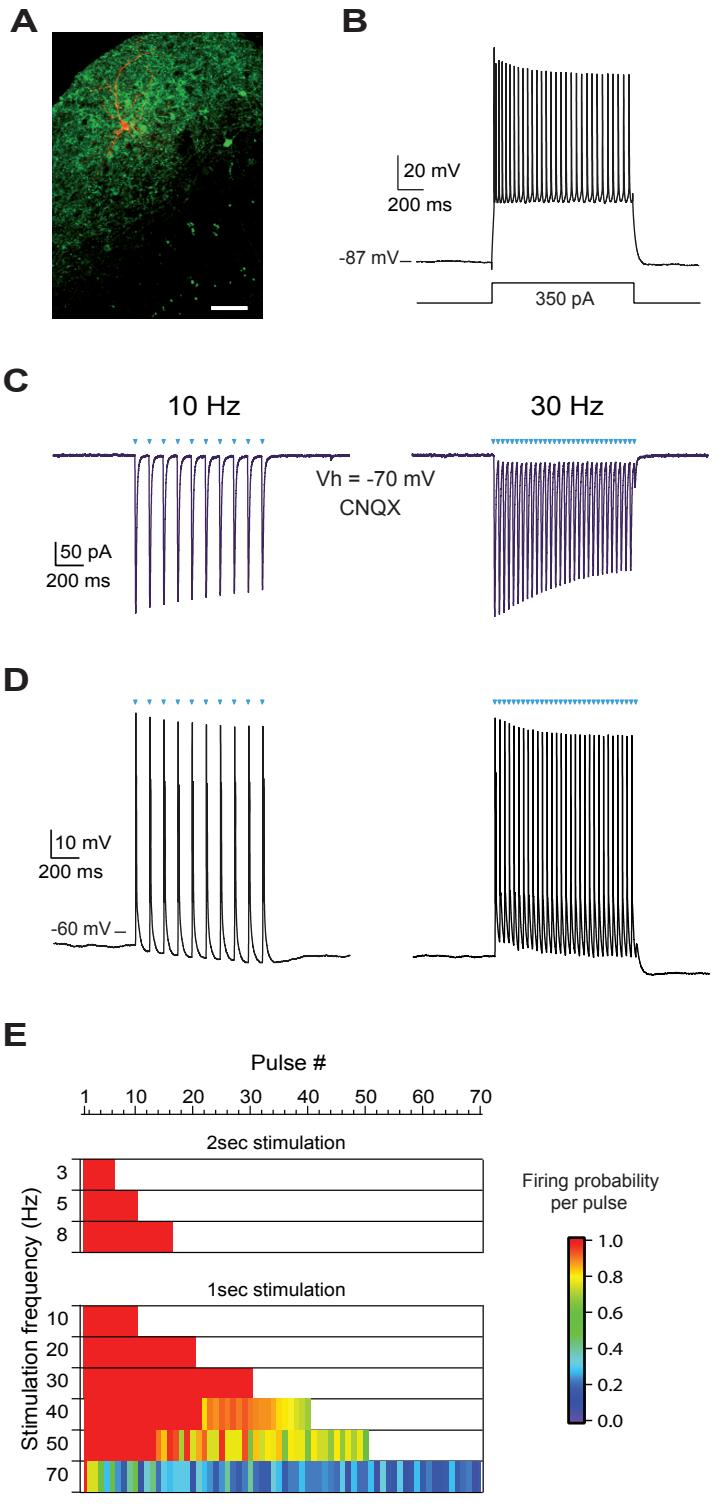
A
B
20 mV
200 ms
-87 mV
350 pA
C
10 Hz
30 Hz
Vh = -70 mV
CNQX
50 pA
200 ms
D
10 mV
200 ms
-60 mV
E
Pulse #
1
10
20
30
40
50
60
70
2sec stimulation
3
5
8
1sec stimulation
10
20
30
40
50
70
Stimulation frequency (Hz)
Firing probability per pulse
1.0
0.8
0.6
0.4
0.2
0.0

Figure S1.

Figure S1. Photostimulation of ChR2-positive neocortical L2/3 pyramidal neurons. Related to Figure 1.

A. High-resolution image showing the biocytin labeling (orange) of an individual L2/3 GFP-positive pyramidal neuron. Scale bar: 50 μm.
B. Regular spiking adapting firing pattern in response to a current pulse for the neuron shown in A.
C. Whole-cell voltage-clamp recording from the neuron shown in A. Light pulses (5ms duration) are indicated by blue ticks.
D. Whole-cell current-clamp recording of the neuron shown in A, revealing its spiking activity in response to the light pulses.
E. Average firing probability in response to light pulses of different frequencies as a function of the pulse number for the population of recorded GFP-positive L2/3 neurons (n=8). Pulse numbers are on the x-axis; stimulation frequency is on the y-axis. Firing probability is color-coded on a linear scale. Photo-stimulations at 3, 5 and 8 Hz were delivered during 2 sec. Photo-stimulations at higher frequencies were delivered during 1 sec.

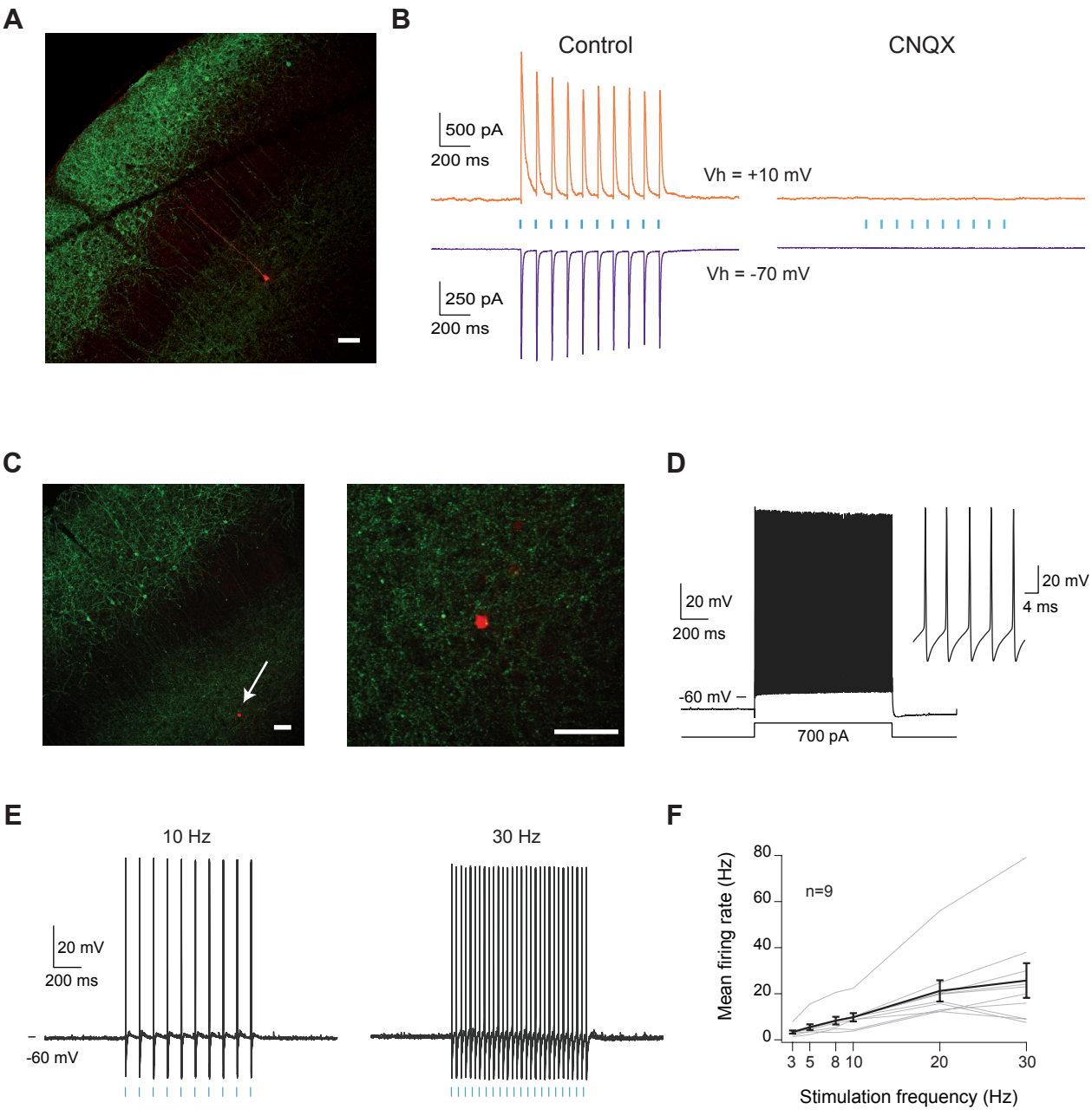
A
B
Control
CNQX
500 pA
200 ms
Vh = +10 mV
Vh = -70 mV
250 pA
200 ms
C
D
20 mV
200 ms
20 mV
4 ms
-60 mV
700 pA
E
10 Hz
30 Hz
20 mV
200 ms
-60 mV
F
n=9
Mean firing rate (Hz)
80
60
40
20
0
3 5 8 10 20 30
Stimulation frequency (Hz)

Figure S2.

Figure S2. Synaptic origin of evoked currents in L5 by photo-stimulation of L2/3 pyramidal neurons. Related to Figure 2.

A. High-resolution image showing the biocytin labeling (red) of an individual L5 pyramidal neuron. Scale bar: 50 μm.
B. Examples of EPSCs (purple traces) and IPSCs (orange traces) evoked in the neuron shown in A by the photostimulation of L2/3 pyramidal neurons at 10 Hz. Note their abolition by the bath applied CNQX (10 μM).
C. High-resolution image showing the biocytin labeling (red) of an individual L5 non-pyramidal neuron. The arrow on the left image points toward the biocytin filled neuron. Right image represents an enlargement of the left one. Scale bars: 50 μm.
D. Fast-spiking non-adapting firing pattern in response to a current pulse for the neuron shown in C.
E. Examples of evoked spiking activity in the neuron shown in C in response to the photostimulation of L2/3 pyramidal neurons.
F. Mean firing rates evoked in L5 fast-spiking neurons as a function of the photostimulation frequency of L2/3 pyramidal neurons. Grey curves correspond to the evoked firing rates in individual neurons, and the black curve corresponds to the average (n=9 neurons). Error bars correspond to +/- SEM.

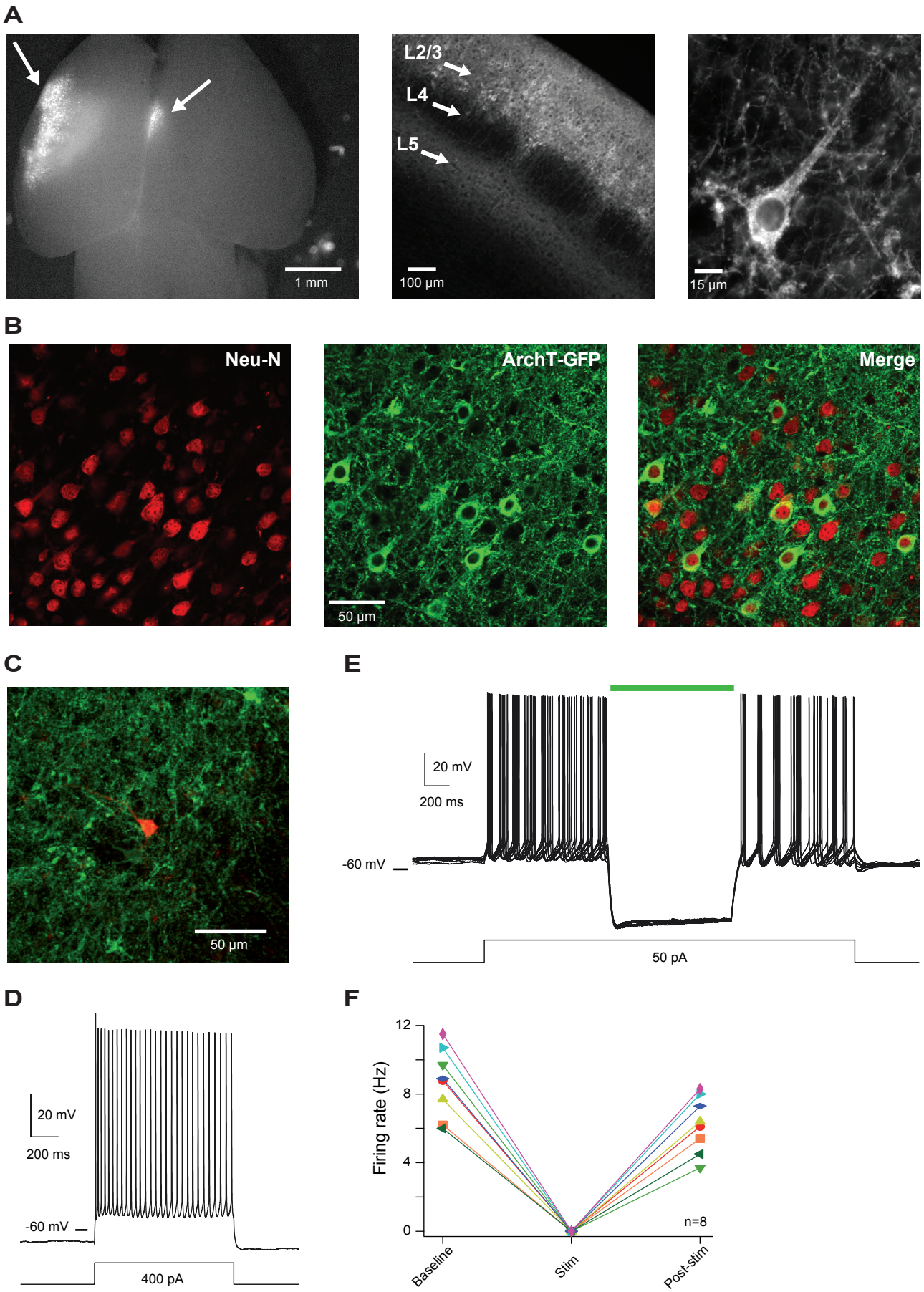
A
1 mm
L2/3
L4
L5
100 µm
15 µm
B
Neu-N
ArchT-GFP
Merge
50 µm
C
50 µm
D
20 mV
200 ms
-60 mV
400 pA
E
20 mV
200 ms
-60 mV
50 pA
F
Firing rate (Hz)
12
8
4
0
n=8
Baseline
Stim
Post-stim

Figure S3.

Figure S3. Photo-inhibition of Arch-positive neocortical L2/3 pyramidal neurons. Related to Figure 3.

A. Left panel: GFP fluorescence in a whole-brain of an electroporated mouse with ArchT-GFP plasmid (scale bar: 1 mm). Arrows indicate S1 (left) and callosal projections (right). Middle panel: GFP fluorescence in a coronal slice through the barrel cortex of an electroporated hemisphere showing somatodendritic labeling in L2/3 and axonal branches in L2/3 and L5 (scale bar: 100 µm). Right panel: labeled L2/3 pyramidal neuron (scale bar: 15 µm).
B. Double immunostaining for ArchT-GFP and the neuronal marker NeuN.
C. High-resolution image showing the biocytin labeling (orange) of an individual L2/3 GFP-positive pyramidal neuron. Scale bar: 50 µm.
D. Regular spiking adapting firing pattern in response to a current pulse for the neuron shown in C.
E. Overlay of membrane potential fluctuations in response to 1-sec green light pulses when the neuron shown in C was held at depolarized membrane potentials (10 trials). Horizontal bar indicates light pulses presentation.
F. Firing rates: before, during and after 1-sec green light pulses for each of the recorded GFP-positive neurons (n=8). Each neuron was held at depolarized membrane potentials before the occurrence of the light pulses.

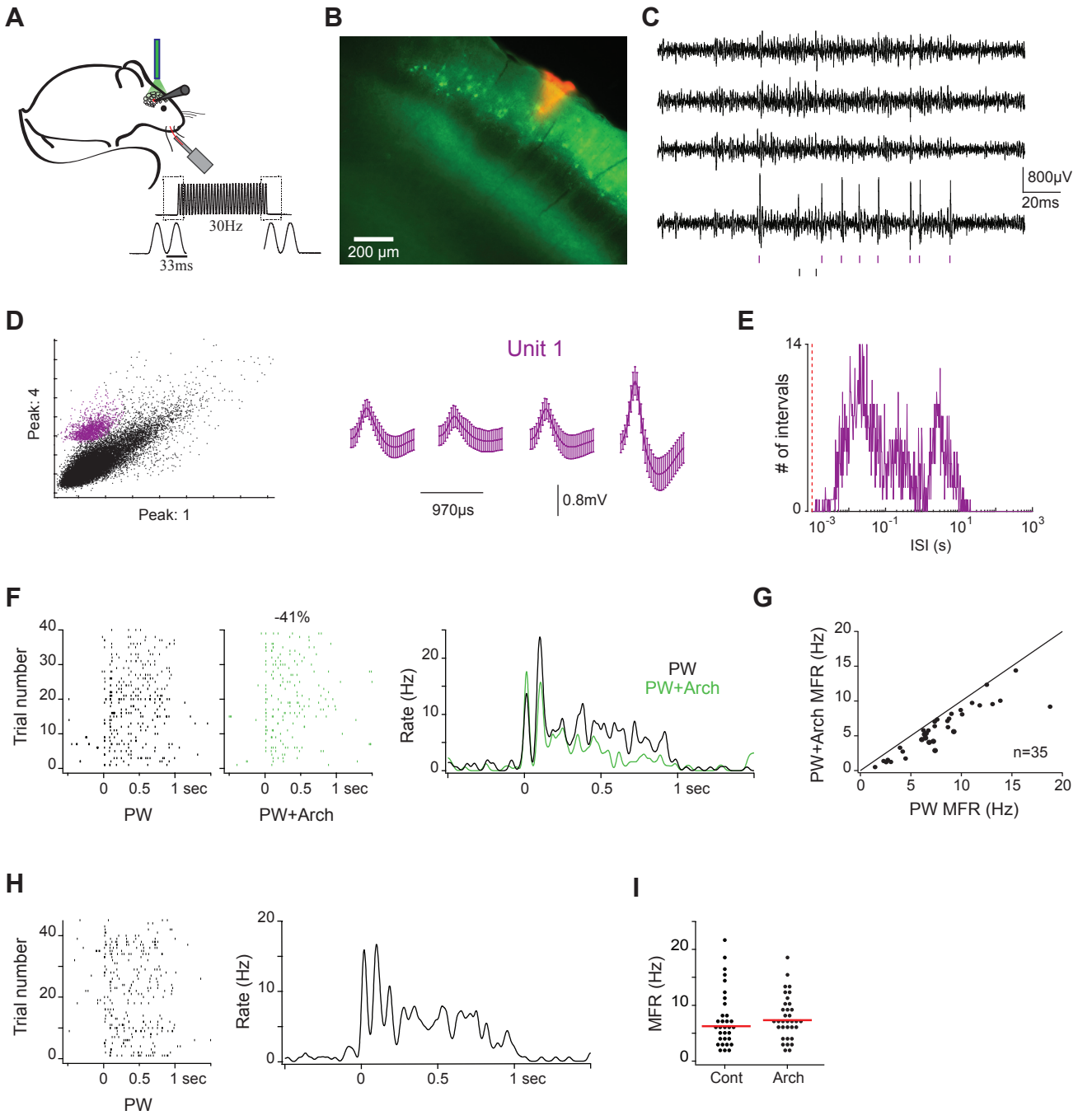
A
30Hz
33ms
B
200 µm
C
800µV
20ms
D
Peak: 4
Peak: 1
Unit 1
970µs
0.8mV
E
# of intervals
ISI (s)
F
Trial number
-41%
PW
PW+Arch
Rate (Hz)
G
PW+Arch MFR (Hz)
PW MFR (Hz)
n=35
H
Trial number
Rate (Hz)
PW
I
MFR (Hz)
Cont
Arch

Figure S4.

Figure S4. Photo-suppression of sensory-evoked spiking activity in L2/3. Related to Figure 3.

A. Schema of the experimental paradigm. Recordings were made in the barrel cortex while stimulating the principal whisker of the recorded units using a piezo-electric device. Top trace represents the stimulus waveform, as measured with photodiodes. Bottom traces represent cutouts of the onset and offset of the stimulus waveform.
B. Example image of a DiI track left by a recording electrode inserted into the barrel cortex. Green: Arch-GFP, red: DiI. Scale bar: 200 μm.
C. Band-pass filtered (0.6–6 kHz) signal from the four wires of a tetrode. Raster plots for one isolated unit (purple) and unclustered spikes (black) are shown at the bottom.
D. Example of a tetrode recording where one unit was isolated. The scatter plots represent the peak amplitudes of spikes on two channels of a tetrode. Assigned spike to one unit are in purple (unassigned spikes are in black). The average waveforms from each of the recording sites for the sorted unit are shown in the right panel.
E. Inter-spike-intervals histograms (ISI) of the clustered unit showing refractory periods. Red line indicates 1 msec ISI.
F. Peri-stimulus time raster plots and histograms of a representative L2/3 unit to 30 Hz whisker stimulations presented either alone (left panel) or paired with green light pulses (middle panel). Stimulations of the principal whisker (PW) start at 0 and last 1 sec. For the raster plots, each line corresponds to one trial and each dot corresponds to the occurrence of an action potential. Note the decrease in the spike count when whisker stimulations are paired with green light pulses.
G. Plot of the evoked mean firing rates (MFR) when sensory stimuli were paired with light pulses (PW+Arch) versus control conditions (PW) for all the recorded units.
H. Peri-stimulus raster plots and histograms of a representative L2/3 unit to 30 Hz whisker stimulations from an unelectroporated animal. Stimulations of the principal whisker (PW) start at 0 and last 1 sec.
I. Scatter plots of the mean firing rates evoked by the stimulation of the principal whisker for the population of recorded single-units from unelectroporated animals (Cont) and electroporated animals (Arch). Horizontal red bars indicate the median values of each distribution.